



Cite this: *Mater. Adv.*, 2022,  
3, 1652

# Optimization of structural expansion and contraction for $\text{TiS}_2$ by controlling the electrochemical window of intercalation/delithiation†

Xue Han,<sup>a</sup> Min Wang,<sup>a</sup> Jingxian Yu<sup>ib</sup> and Shengping Wang<sup>id</sup>\*<sup>a</sup>

A reversible layered structure of  $\text{TiS}_2$  with relaxation like a spring, can be achieved by controlling the optimized potential range to 0.9–2.8 V (vs.  $\text{Li}^+/\text{Li}$ ) to yield a high discharge capacity, long cycling life, and excellent rate performance. The discharge capacity density and Coulombic efficiency for  $\text{TiS}_2$  at the 100th cycle at 0.1  $\text{mA cm}^{-1}$  and 0.9–2.8 V are 321  $\text{mA h g}^{-1}$  and ~100%, respectively, which are more effective and better than those over potential ranges of 0.8–2.8 V and 1.0–2.8 V. In response to this, the deeper lithiation of  $\text{TiS}_2$  at 0.8 V leads to the formation of irreversible  $\text{Ti}_2\text{S}$  and results in poor cycling performance. The reduced lithiation of  $\text{TiS}_2$  at 1.0 V results in low capacity density. Therefore, the relationship between the lithiation depth, structural stability, and electrochemical characteristics of  $\text{TiS}_2$  as an electrode material is clarified. Controlling the optimized potential range for structural stability during discharge/charge is thus an effective way of improving electrochemical performance.

Received 29th September 2021,  
Accepted 12th December 2021

DOI: 10.1039/d1ma00900a

rsc.li/materials-advances

## 1 Introduction

The electrode materials of lithium-ion batteries (LIBs) determine the energy density and power density of the cells.<sup>1–3</sup>  $\text{TiS}_2$  as an anode material with a four-electron electrochemical reaction demonstrates a high theoretical capacity density of 956  $\text{mA h g}^{-1}$ .<sup>4,5</sup> The interlayer spacing (5.703 Å) of  $\text{TiS}_2$  with a layered structure is greater than that (3.4 Å) of graphite.<sup>6,7</sup> Therefore,  $\text{TiS}_2$  exhibits rapid intercalation/deintercalation and diffusion of lithium ions, and good electronic conductivity.<sup>8</sup> Therefore,  $\text{TiS}_2$  has great potential for application as an electrode material.

In LIBs, the lithiation/delithiation of  $\text{TiS}_2$  can be divided into two processes (Equation (S1) and (S2), ESI†).<sup>9</sup> The discharge potential of  $\text{TiS}_2$  is higher than 1.4 V, and a small amount of lithium ions intercalate the  $\text{TiS}_2$  layers and form  $\text{Li}_x\text{TiS}_2$  ( $0 < x \leq 1$ ). In this process, which is a typical solid solution reaction, the electrode materials exhibit good reversibility. As additional lithium ions intercalate into the  $\text{Li}_x\text{TiS}_2$  ( $1 < x \leq 4$ ),  $\text{TiS}_2$  gradually transforms into  $\text{Li}_2\text{S}$  and Ti, and the layered structure is destroyed. Excessive lithium intercalation

of  $\text{TiS}_2$  causes fracturing of the crystal structure and reduces the cycling stability of the material.<sup>10</sup> Therefore, the incompatibility of the capacity density and cycling performance of  $\text{TiS}_2$  is a key issue.  $\text{TiS}_2$  with a special morphology, and its composites with other materials, can be effectively used to improve electrochemical performance, but most of these synthesis processes are complex and difficult.<sup>11,12</sup> Therefore, it is extremely important to find a simple and convenient way to achieve produce  $\text{TiS}_2$  that exhibits both a high capacity density and long cycling life.

In previous studies on sulfur<sup>13,14</sup> and  $\text{MnO}_2$ ,<sup>15</sup> it was found that by controlling the discharge/charge potential range of the electrode materials, their cycling lives and capacity densities could be improved. This suggests that it may be possible to achieve increased capacity density and cycling performance by adjusting the lithiation depth of  $\text{TiS}_2$ . Obviously, if the critical point of the stable layered structure of  $\text{TiS}_2$  during discharge/charge is found, these goals could be achieved. Therefore, the evolution of the crystal structure during discharge/charge and the relationships between the electrochemical window, capacity density and cycling life need to be studied in depth.

In this paper, based on powder X-ray diffraction (XRD), selected area electron diffraction (SAED), and electrochemical methods, the lithiation/delithiation processes of  $\text{TiS}_2$  over various potential ranges were systematically studied. It was found that lithium ions intercalate to generate  $\text{Ti}_2\text{S}$  after a series of phase transitions ( $\text{TiS}_2$ – $\text{LiTiS}_2$ – $\text{Ti}_2\text{S}$ ). The formation of irreversible  $\text{Ti}_2\text{S}$  results in  $\text{TiS}_2$  being produced over 0.8–2.8 V,

<sup>a</sup> Faculty of Materials Science and Chemistry, China University of Geosciences, Wuhan 430074, China. E-mail: spwang@cug.edu.cn

<sup>b</sup> ARC Centre of Excellence for Nanoscale BioPhotonics (CNBP), School of Chemistry and Physics, The University of Adelaide, Adelaide, SA 5005, Australia

† Electronic supplementary information (ESI) available. See DOI: 10.1039/d1ma00900a

which promotes poor cycling performance. Therefore, by controlling the potential window to 0.9–2.8 V, the formation of  $\text{Ti}_2\text{S}$  is avoided, and the Coulombic efficiency and cycling life of  $\text{TiS}_2$  are improved. This represents a new approach for enhancing the lithium storage performance of layered transition metal sulfides.

## 2 Results and discussion

### 2.1 Morphology and crystal structure

As shown in Fig. S1 (ESI<sup>†</sup>), the diffraction peaks of the sample are consistent with hexagonal  $\text{TiS}_2$  (PDF#15-0853). However, it is important to note that the intensity ratios of the (101) and (001) peaks in this work are quite different from those of the standard diffraction pattern. The (001) peak intensity is the strongest among the diffraction peaks. During Rietveld refinement, the preferred orientation was carefully considered, and this was an important step in improving the fitting and minimizing the difference. This result suggests a preferential orientation of the (001) plane of  $\text{TiS}_2$ .<sup>16</sup>  $\text{TiS}_2$  has a typical layered structure, with each layer composed of two hexagonal close-packed S atoms. Ti is located in the center to form an octahedron. The layers of  $\text{TiS}_2$  are connected *via* weak van der Waals forces with a layer spacing of 5.691 Å.<sup>17</sup>  $\text{TiS}_2$  has two active sites (octahedral and tetrahedral) for lithium ion storage.<sup>18,19</sup> Scanning electron microscopy (SEM) and transmission electron microscopy (TEM) images indicate that  $\text{TiS}_2$  comprises oval flakes with a particle size of  $\sim 300$  nm (Fig. S2, ESI<sup>†</sup>).

### 2.2 Electrochemical performance

**2.2.1 Cycling performance.** The galvanostatic discharge/charge (GDC) curves of the samples with various electrochemical windows are shown in Fig. S3a and b (ESI<sup>†</sup>). The capacity densities for the first and 50th discharges over 0.01–2.8 V are 1527 and 19 mA h g<sup>−1</sup>, respectively. Based on early studies, the low capacity retention rate is possibly due to the volumetric expansion of crystals during lithium intercalation/deintercalation, which causes the fracturing of crystals.<sup>10</sup> The capacity density for  $\text{TiS}_2$  after the 50th discharge over a potential range of 1.5–2.8 V is 189 mA h g<sup>−1</sup> and 88.9% of the first discharge capacity is retained. Obviously, the cycling performance of  $\text{TiS}_2$

over 1.5–2.8 V is better than that over 0.01–2.8 V.  $\text{TiS}_2$  with deep lithiation converted to  $\text{Li}_2\text{S}$  and Ti. Excessive lithiation caused volumetric expansion and even crystal crushing, leading to poor cycling performance.

This work aimed to clarify the threshold of the electrochemical windows at which  $\text{TiS}_2$  could maintain its layered structure and exhibit excellent cycling stability. A wide window (*e.g.*, 0.01–2.80 V) with high specific capacity and poor cycling stability and a narrow window (*e.g.*, 1.50–2.80 V) with low specific capacity and good cycling stability are compared in Fig. S3c (ESI<sup>†</sup>). The results urged us to think about the threshold of the electrochemical windows in terms of both good cycling stability and high specific capacity. Based on these results, it was necessary for us to conduct full research to identify this threshold.

The ratio of the actual capacity density to the theoretical capacity density of  $\text{TiS}_2$  from 1.5–2.8 V is 0.79, therefore  $\sim 0.79$  mol lithium ions are intercalated in  $\text{TiS}_2$  when it is discharged to 1.5 V. The good cycling performance of  $\text{TiS}_2$  over 1.5–2.8 V indicates that its crystal structure is reversible and stable during lithiation/delithiation. Comparing the capacity density and cycling performance of  $\text{TiS}_2$  over various potential ranges, it was observed that  $\text{TiS}_2$  with a narrow potential range exhibits increased cycling performance and decreased capacity density.  $\text{TiS}_2$  with a wide potential range exhibits increased capacity density and poor cycling performance. Therefore, it is necessary to find a suitable discharge/charge potential window for  $\text{TiS}_2$  to exhibit both a long cycling life and high capacity density.

The cycling characteristics of  $\text{TiS}_2$  over various potential ranges are shown in Fig. 1a.  $\text{TiS}_2$  over 0.9–2.80 V exhibits excellent cycling performance, with discharge capacity densities of the first and 100th cycles of 321 and 213 mA h g<sup>−1</sup>, respectively. The Coulombic efficiency at the 100th cycle is close to 100%. The discharge capacity density and Coulombic efficiency after 100 cycles for  $\text{TiS}_2$  from 0.8–2.8 V are 58 mA h g<sup>−1</sup> and 90%, respectively, and the capacity density is far lower than that of the first cycle (405 mA h g<sup>−1</sup>). Obviously,  $\text{TiS}_2$  with a potential range of 0.9–2.8 V exhibits the best electrochemical performance. This is related to the structural evolution of  $\text{TiS}_2$  during lithiation/delithiation.

**2.2.2 dQ/dV curves.** The dQ/dV curves of  $\text{TiS}_2$  for the 25th GDC curves are shown in Fig. 1b. The dQ/dV curves over

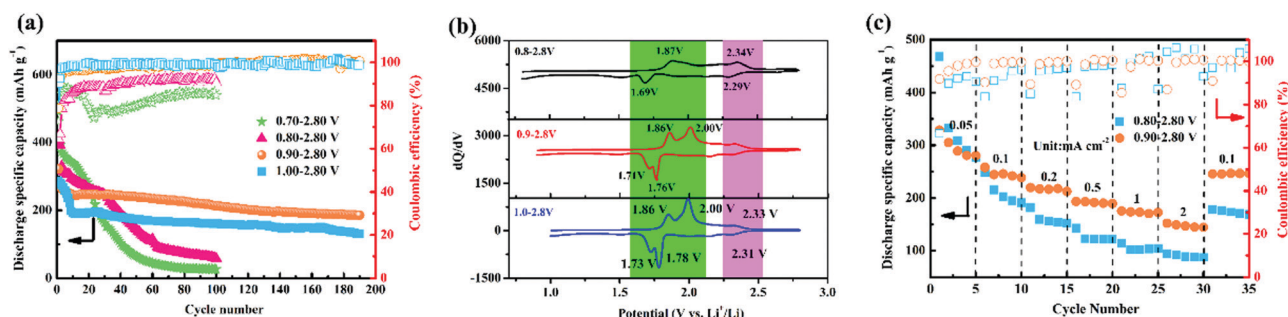


Fig. 1 (a) Cycling performance at 0.1 mA cm<sup>−2</sup>, (b) dQ/dV curves of the 25th discharge/charge curves at 0.1 mA cm<sup>−2</sup>, and (c) the rate performance of  $\text{TiS}_2$  across various electrochemical windows.

0.8–2.8 V exhibit two pairs of redox peaks at 2.29/2.34 V and 1.69/1.87 V with differential capacitances of 170.64/322.33 and 362.36/377.11 mA h g<sup>-1</sup> V<sup>-1</sup>, respectively. The dQ/dV curves over 0.9–2.8 V exhibit two pairs of redox peaks at 2.31/2.34 V and 1.71/2.01 V with differential capacitances of 134.83/221.21 and 585.67/750 mA h g<sup>-1</sup> V<sup>-1</sup>, respectively. The dQ/dV curves of 1.0–2.8 V exhibit two pairs of redox peaks at 2.31/2.33 V and 1.73/2.00 V with differential capacitances of 151.68/176.97 and 703.65/994.38 mA h g<sup>-1</sup> V<sup>-1</sup>, respectively. These peaks in the dQ/dV curves at ~2.31/~2.34 V and ~1.71/~1.86 V indicate that lithium ions intercalate in (delithiated from) TiS<sub>2</sub> to form Li<sub>x</sub>TiS<sub>2</sub> (0 < x ≤ 1).<sup>9</sup> The smaller differences in the redox peak potentials at ~2.31/~2.34 V and ~1.71/~1.86 V show that the reversibilities of the discharge/charge reactions over 0.9–2.8 V and 1.0–2.8 V are better than those over 0.8–2.8 V. The currents of the redox peaks also support this conclusion.

The dQ/dV curves over 0.9–2.8 V and 1.0–2.8 V feature another pair of redox peaks at ~1.76/~1.86 V, which indicates an additional lithiation/delithiation process for Li<sub>x</sub>TiS<sub>2</sub> (0 < x ≤ 1). However, there are no corresponding peaks at ~1.76/~1.86 V in the dQ/dV curves over 0.8–2.8 V, which indicates that the TiS<sub>2</sub> crystal undergoes an irreversible phase transition when discharged at 0.8 V. Obviously, this crystal structure and phase change affect the electrochemical behavior during the discharge/charge processes below 0.9 V.

**2.2.3 Rate performance.** The rate performance of TiS<sub>2</sub> over various potential ranges is shown in Fig. 1c. TiS<sub>2</sub> over 0.9–2.8 V exhibits good rate performance, with discharge capacities at 0.05, 0.1, 0.2, 0.5, 1, 2, and 0.1 mA cm<sup>-2</sup> of 325, 240, 215, 190, 170, 145, and 250 mA h g<sup>-1</sup>, respectively. In contrast, its rate performance over 0.8–2.8 V is poor, and its discharge capacity and Coulombic efficiency at 2 mA cm<sup>-2</sup> are 85 mA h g<sup>-1</sup> and 55%, respectively. Therefore, by controlling the potential range

of TiS<sub>2</sub> to 0.9–2.8 V, not only does this improve the capacities, but the reversibility of the lithiation/delithiation is also promoted.

**2.2.4 Cyclic voltammetry (CV) curves.** The first CV curves of TiS<sub>2</sub> over 0.8–2.8 V exhibit reduction peaks at 1.19, 1.39, 1.64, 1.75, 2.08, and 2.33 V (Fig. 2a). These reduction peaks correspond to the formation of Li<sub>x</sub>TiS<sub>2</sub> (0 < x ≤ 1).<sup>9</sup> The oxidation peaks of over 1.5 V correspond to the step-by-step delithiation process. There are no reduction peaks at ~1.75 V and an oxidation peak at ~1.88 V in the second CV curve, indicating that TiS<sub>2</sub> undergoes an irreversible phase transition after the first cycle. These results from the CV curves over 0.8–2.8 V are consistent with those from the dQ/dV curves (Fig. 1b) and GDC curves (Fig. 2b). The first discharge capacity density and the coulombic efficiency of TiS<sub>2</sub> over 0.8–2.8 V are 270 mA h g<sup>-1</sup> and 63.8%, respectively. The low Coulombic efficiency might be attributed to electrolyte decomposition and the formation of solid electrolyte interface (SEI) films.<sup>9</sup> The capacity degradation mainly occurs in the range of 1.5–2.0 V. In the following cycle, the plateau of the GDC curve weakens and gradually takes the form of an inclined line. The CV data show a similar trend, and the currents for the redox peaks of CV in the range of 1.5–2.0 V decrease with increasing cycle number.

The redox peaks of TiS<sub>2</sub> over 0.9–2.8 V can still be observed at ~1.75/~1.88 V in the following CV curve (Fig. 2c), and their peak currents increase with increasing cycle number. Therefore, the crystal structure of TiS<sub>2</sub> during GDC in the range of 0.9–2.8 V is reversible, and the GDC curves also show the same phenomenon (Fig. 2d). The plateau length of the discharge curve elongates with increasing cycle number, and the plateau potential of 1.71 V is higher than the potential that reaches 1.69 V over 0.8–2.8 V. The CV and GDC curves in the range of 1.0–2.8 V are similar to those in the range of 0.9–2.8 V

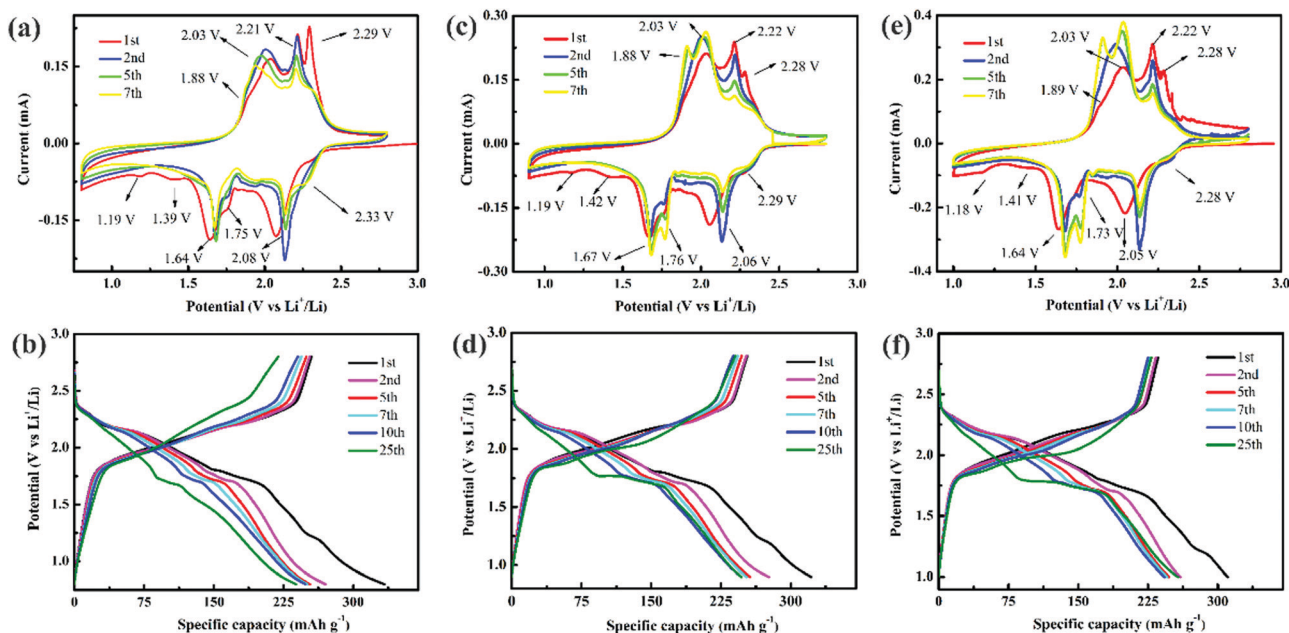


Fig. 2 CV curves at 0.1 mV s<sup>-1</sup> and discharge/charge curves at 0.1 mA cm<sup>-2</sup> of TiS<sub>2</sub> over (a and b) 0.8–2.8 V, (c and d) 0.9–2.8 V, and (e and f) 1.0–2.8 V.



(Fig. 2e and f), indicating that they show the same lithium storage behavior.

## 2.3 Electrochemical reaction kinetics

**2.3.1 Diffusion coefficient.** The lithium ion diffusion coefficient ( $D_{\text{Li}^+}$ ) of  $\text{TiS}_2$  from the open circuit voltage (OCV) to 0.01 V during the first discharge process was studied by galvanostatic intermittent titration (GITT), where  $D_{\text{Li}^+}$  was calculated using eqn (S3) (ESI<sup>†</sup>).<sup>20,21</sup> As shown in Fig. S4 (ESI<sup>†</sup>),  $D_{\text{Li}^+}$  shows an increasing trend during the initial discharge stage (1.92–0.9 V), and reaches a maximum value at 0.9 V (except for the initial stage) as the lithium ions mainly intercalate within the interlayers of the  $\text{TiS}_2$ . The interlayer distance of  $\text{TiS}_2$  increases, and the energy barrier for lithium ion diffusion is reduced. The discharge potential is lower than 0.9 V, and additional lithium ions are inserted into the  $\text{Li}_x\text{TiS}_2$  ( $0 < x \leq 1$ ), and some of the  $\text{Li}_x\text{TiS}_2$  ( $0 < x \leq 1$ ) undergoes a conversion reaction. The layered structure is destroyed by the large interfacial stress resulting from the transformation reaction. At this time, lithium ion diffusion requires a higher energy barrier, so  $D_{\text{Li}^+}$  decreases as the depth of discharge (DOD) increases.

**2.3.2 Impedance evolution.** The decay mechanism of  $\text{TiS}_2$  over 0.8–2.8 V during GDC was explored using EIS with an equivalent circuit diagram (Fig. S5, ESI<sup>†</sup>), which features solution resistance ( $R_s$ ), charge transfer resistance ( $R_{\text{ct}}$ ), and SEI resistance ( $R_{\text{SEI}}$ ).<sup>22</sup> The semicircle in the high-frequency region is dominated by the charge transfer process, and the diameter of the semicircle represents  $R_{\text{ct}}$ , which indicates that

the process is kinetically controlled. The spectrum in the low-frequency region has the appearance of a straight line, which indicates that the process is a diffusion controlled.<sup>23</sup>

The first discharge/charge curves and EIS curves of  $\text{TiS}_2$  at various DODs and depths of charge (DOCs) are shown in Fig. S6 (ESI<sup>†</sup>). The  $R_{\text{ct}}$  value gradually decreases during the discharge process and increases during the charge process (Fig. 3a and b), and the  $R_{\text{ct}}$  is related to the lithium molar content in  $\text{TiS}_2$ . The  $R_{\text{SEI}}$  gradually increases during the early discharge stage, which means that the SEI film is continuously generated. The  $R_{\text{SEI}}$  value of  $\text{TiS}_2$  at a DOD of approximately 50% ( $\sim 0.8$  V vs  $\text{Li}^+/\text{Li}$ ) is at a maximum, which indicates that the SEI film on the electrode surface is unstable.

The EIS curves of  $\text{TiS}_2$  from discharge to the cutoff potential (0.8 or 0.9 V) and charge to 2.8 V are shown in Fig. S7 (ESI<sup>†</sup>). The SEI film over 0.9–2.8 V was generated during the first discharge and basically remained stable throughout the cycle process (Fig. 3c and d). The  $R_{\text{ct}}$  of the regions 0.8–2.8 V and 0.9–2.8 V gradually decrease with increasing cycle number, which is related to the electrode active material. The exchange current density at 0.9–2.8 V is higher than that at 0.8–2.8 V, indicating that  $\text{TiS}_2$  at 0.9–2.8 V shows improved reversibility for a low  $R_{\text{ct}}$  value and a stable SEI film (Fig. S8, ESI<sup>†</sup>).

**2.3.3 Capacity contribution mechanism.** The characteristic CV values for  $\text{TiS}_2$  at various scan rates were obtained using Equation (S4)–(S7) (ESI<sup>†</sup>), which were used to determine the capacity contribution mechanism of  $\text{TiS}_2$  at 0.8–2.8 V and 0.9–2.8 V.<sup>24,25</sup> The two CV curves exhibit similar shapes, and

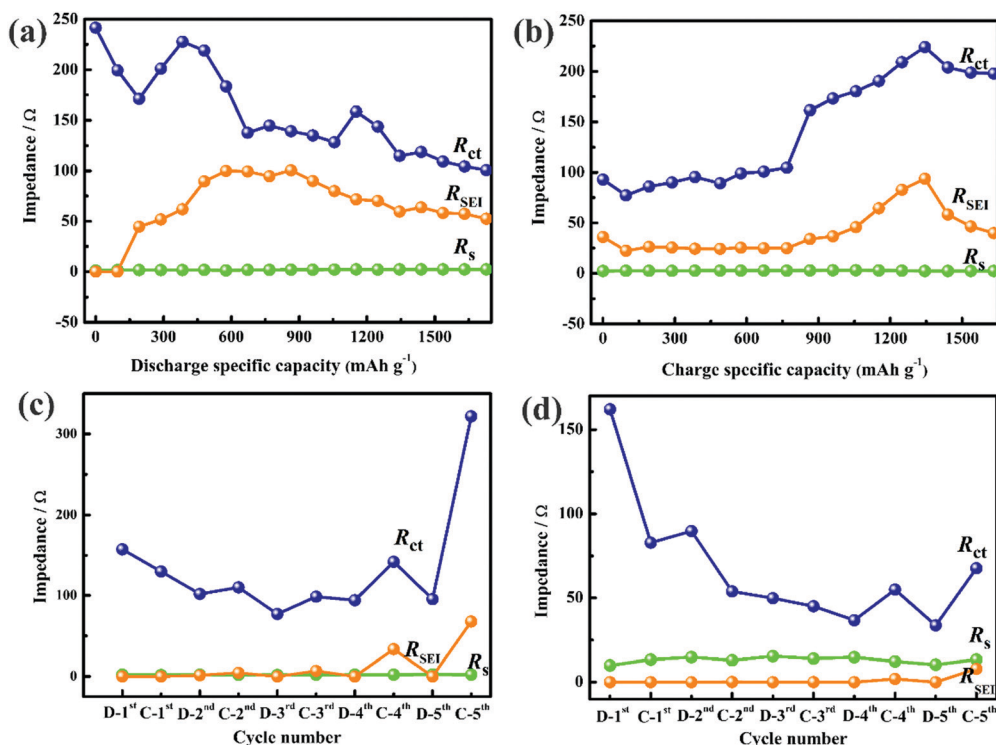


Fig. 3 Impedances of  $\text{TiS}_2$  at various (a) DODs and (b) DOCs during the first discharge/charge processes and at full states of discharge/charge for various cycles over (c) 0.8–2.8 V and (d) 0.9–2.8 V.



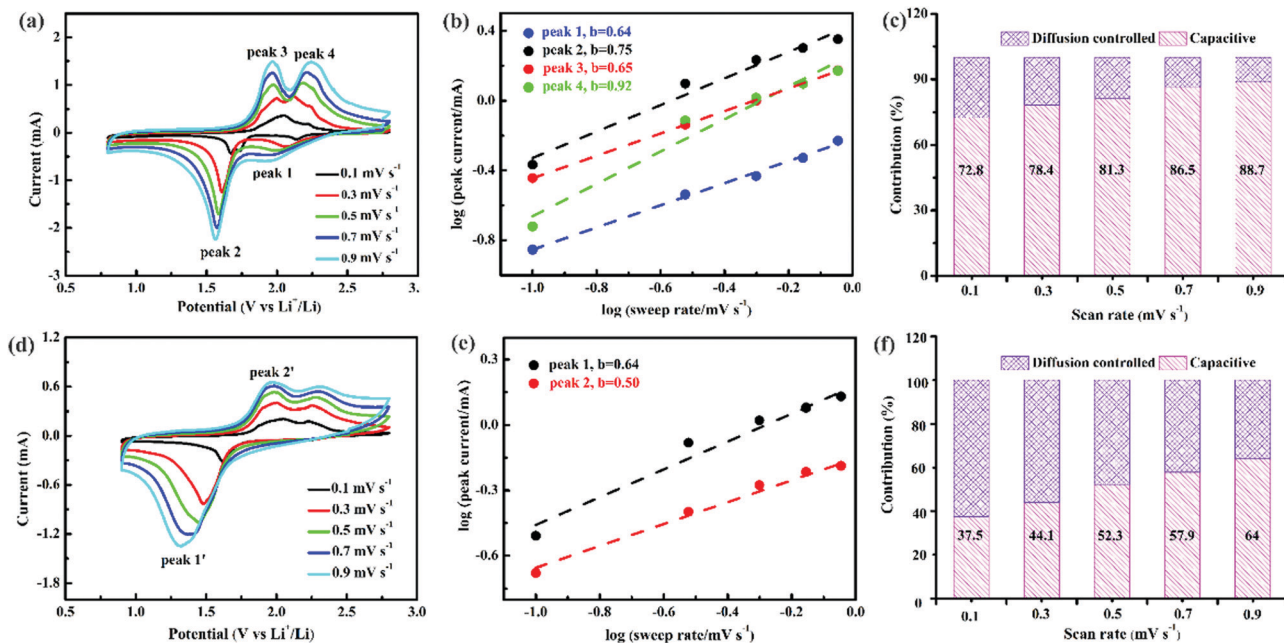


Fig. 4 CV curves,  $b$  values, and capacity ratio of the capacitive (blue) and diffusion-controlled (pink) processes  $\text{TiS}_2$  at (a–c) 0.8–2.8 V and (d–f) 0.9–2.8 V.

the current intensities of the redox peaks increase with an increase in the scan rate (Fig. 4).

The  $b$  values of the reduction and oxidation peaks of  $\text{TiS}_2$  at 0.9–2.8 V are 0.64 and 0.50, respectively. Therefore, the electrochemical reaction of  $\text{TiS}_2$  at 0.9–2.8 V is mainly diffusion controlled. Simultaneously, the capacity ratio for the capacitive behavior of  $\text{TiS}_2$  increases from 37.5% to 64% upon an increase in the scan rate (Fig. 4a–c). The  $b$  values of the reduction and oxidation peaks of  $\text{TiS}_2$  at 0.8–2.8 V are 0.64/0.75 and 0.65/0.92, respectively, and the corresponding electrochemical reactions are dominated by capacitance and diffusion. The proportion of capacitive behavior increases from 72.8% to 88.7% upon an increase in the scan rate (Fig. 4d–f), which is higher than that at 0.9–2.8 V. It is generally believed that capacitive behavior accelerates the kinetics of electrochemical reactions.<sup>26</sup> Therefore, the key factor is not the contribution of capacitive behavior, but the integrity of the  $\text{TiS}_2$  crystal structure during GDC that led to the excellent rate performance of  $\text{TiS}_2$  at 0.9–2.8 V.

#### 2.4 Lithium storage mechanism

The above results show that  $\text{TiS}_2$  at 0.9–2.8 V shows improved cycle life and capacity density, and that the poor cycling performance of  $\text{TiS}_2$  at 0.8–2.8 V is due to the irreversible phase transition of the layered structure (Table S1, ESI†). The XRD patterns of  $\text{TiS}_2$  at various DODs and DOCs are shown in Fig. 5a–c. Lattice expansion is observed from the XRD patterns. The  $c$  value of the  $\text{TiS}_2$  unit cell during discharge at points A ( $\text{TiS}_2$ , 2.68 V), B ( $\text{Li}_{0.18}\text{TiS}_2$ , 2.10 V), and C ( $\text{Li}_{0.68}\text{TiS}_2$ , 1.76 V) are 5.69, 5.83 and 6.29 Å, respectively. During the initial discharge process, lithium ions intercalate in the interlayers of  $\text{TiS}_2$ , occupying the octahedral position and resulting in a significant increase in the interlayer distance.<sup>27</sup> The layered structure shows excellent reversibility for a charge/discharge process, as

evidenced by the shift in the (001) peak. The characteristic peak for  $\text{Ti}_2\text{S}$  is also observed when discharged to point E. During the charge process from point E to point H, the peak intensities of  $\text{Ti}_2\text{S}$  decrease with increasing DOC, but these peaks do not completely disappear. Therefore, the irreversible  $\text{Ti}_2\text{S}$  produced by the partial conversion reaction is the reason for the poor cycling performance of  $\text{TiS}_2$  at 0.8–2.8 V. The layered-structure of the original  $\text{TiS}_2$  can be retained by carefully controlling the lithiation depth, *e.g.*, setting a rational electrochemical window of 0.9–2.8 V. A further discharge process leads to an irreversible  $\text{Ti}_2\text{S}$ , therefore resulting in poor cycling stability.<sup>28</sup>

The SAED results of  $\text{TiS}_2$  during GDC are shown in Fig. 5d–i. The original  $\text{TiS}_2$  exhibits a typical 1H structure, and the diffraction spots are arranged symmetrically in a hexagon, which indicates that it is single crystalline in nature.<sup>29</sup> The interlayer spacing of  $\text{TiS}_2$  upon discharge to 0.9 V increases for the formation of  $\text{Li}_x\text{TiS}_2$ , and the layered structure is not destroyed (Fig. 5d). Upon discharge to 0.8 V, the electron diffraction pattern changes from diffraction spots to diffraction rings, which indicates that the material is polycrystalline (Fig. 5i). Simultaneously, new diffraction rings appear with interplanar spacings of 2.15 Å and 1.36 Å, related to the (051) and (062) planes of  $\text{Ti}_2\text{S}$ , which are consistent with the XRD results. A deep discharge of  $\text{TiS}_2$  causes it to undergo a conversion reaction.

Theoretical calculations were employed to further investigate the structural evolution. The geometries of  $\text{Li}_x\text{TiS}_2$  ( $x = 0–3$ ) were optimized using the SIESTA 4.0 package, and the results are shown in Fig. S10 (ESI†). The expansion in the volume is only 4.5% when one  $\text{Li}^+$  is inserted into the structure, while an approximately 15.5% change occurs on going from  $\text{LiTiS}_2$  to  $\text{Li}_2\text{TiS}_2$ . This result means that  $\text{Li}_2\text{TiS}_2$  is unable to maintain its original structure due to drastic structural changes. These results are consistent with the

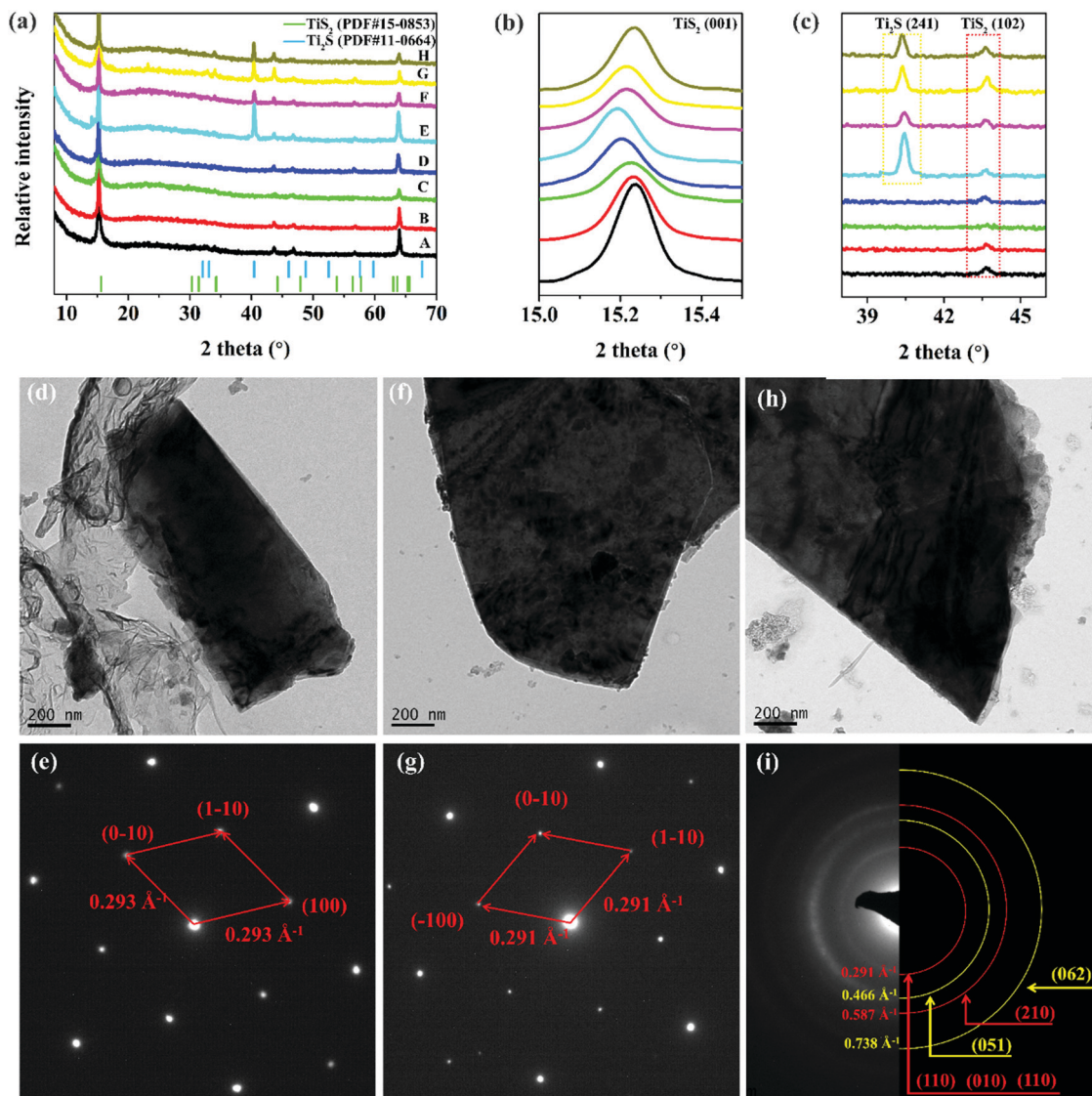


Fig. 5 (a–c) *Ex situ* XRD results at different states collected from Fig. S9 (ESI†). TEM and SAED images of TiS<sub>2</sub> at (d and e) the initial state, and upon discharge to (f and g) 0.9 V and (h and i) 0.8 V.

experiment values. The irreversible Ti<sub>2</sub>S phase was identified by XRD and SAED when 2 Li<sup>+</sup> ions were inserted into TiS<sub>2</sub>.

Here, we provide a detailed summary of the structural evolution of TiS<sub>2</sub>. The layer spacings of pristine TiS<sub>2</sub> and at 0.9 V are 5.70 Å and 5.81 Å. Upon discharge to 0.8 V, a new phase comprising Ti<sub>2</sub>S is generated, and the layered structure is destroyed. At 0.01 V, Li<sub>2</sub>S and Ti are produced in a conversion reaction. Over the optimized potential window of 0.9–2.8 V, TiS<sub>2</sub> retains its layered structure, therefore exhibiting excellent cycling capability. The irreversible Ti<sub>2</sub>S at 0.8–2.8 V leads to increased capacity density and reduced cycling performance of TiS<sub>2</sub>.

### 3 Conclusions

The layered structure of TiS<sub>2</sub> over an optimized potential range of 0.9–2.8 V is retained, and the goals of high capacity density,

long cycling life, and excellent rate performance were achieved. The discharge capacity density and Coulombic efficiency of the 100th cycle at 0.1 mA cm<sup>-2</sup> are 321 mA h g<sup>-1</sup> and ~100%, respectively. TiS<sub>2</sub> upon discharge to 0.8 V generates Ti<sub>2</sub>S in a conversion reaction, and the irreversible Ti<sub>2</sub>S leads to poor cycling performance. The discharge capacity of TiS<sub>2</sub> at 0.8–2.8 V for the 100th cycle is only 58 mA h g<sup>-1</sup>.

Controlling the potential range of TiS<sub>2</sub> during discharge/charge could thus be used to improve the Coulombic efficiency and cycling life of other layered electrode materials, making it an effective and simple method to achieve excellent electrochemical performance of materials by adjusting the depth of lithiation.

### Conflicts of interest

There are no conflicts to declare.

## Acknowledgements

The work was supported by the Key Research and Development Program of Hubei Province, China (2020BHB013). The computational aspects of this work were supported by an award under the National Computational Merit Allocation Scheme for J. Y. on National Computing Infrastructure (NCI) at Australian National University and Pawsey Supercomputing Centre in Western Australia.

## References

- 1 M. Li, J. Lu, Z. Chen and K. Amine, 30 years of lithium-ion batteries, *Adv. Mater.*, 2018, **30**, 1800561, DOI: 10.1002/adma.201800561.
- 2 G. Zhu, L. Wang, H. Lin, L. Ma, P. Zhao, Y. Hu, T. Chen, R. Chen, Y. Wang, Z. Tie, J. Liu and Z. Jin, Walnut-like multicore-shell MnO encapsulated nitrogen rich carbon nanocapsules as anode material for long cycling and soft-packed lithium-ion batteries, *Adv. Funct. Mater.*, 2018, **28**, 1800003, DOI: 10.1002/adfm.201800003.
- 3 X. Chen, G. Ge, W. Wang, B. Zhang, J. Jiang, X. Yang, Y. Li, L. Wang, X. He and Y. Sun, In situ formation of ionically conductive nanointerphase on Si particles for stable battery anode, *Sci. China: Chem.*, 2021, **64**, 1417–1425, DOI: 10.1007/s11426-021-1023-4.
- 4 M. Fu, Z. Yao, X. Ma, H. Dong, K. Sun, S. Hwang, E. Hu, H. Gan, Y. Yao, E. A. Stachet, C. Wolverton and D. Su, Expanded lithiation of titanium disulfide: reaction kinetics of multi-step conversion reaction, *Nano Energy*, 2019, **63**, 103882, DOI: 10.1016/j.nanoen.2019.103882.
- 5 S.-Y. Chen, Z.-X. Wang, X.-P. Fang, H.-L. Zhao, X.-J. Liu and L.-Q. Chen, Characterization of TiS<sub>2</sub> as an anode material for lithium ion batteries, *Acta Phys.-Chim. Sin.*, 2011, **27**, 97–102, DOI: 10.3866/PKUWHXB20110134.
- 6 A. H. Whitehead, K. Edström, N. Rao and J. R. Owen, *In situ* X-ray diffraction studies of a graphite-based Li-ion battery negative electrode, *J. Power Sources*, 1996, **63**, 41–45, DOI: 10.1016/S0378-7753(96)02440-8.
- 7 K. Toyoura, Y. Koyama, A. Kuwabara and I. Tanaka, Effects of off-stoichiometry of LiC<sub>6</sub> on the lithium diffusion mechanism and diffusivity by first principles calculations, *J. Phys. Chem. C*, 2010, **114**, 2375–2379, DOI: 10.1021/jp910134u.
- 8 H. Wang, Z. Qiu, W. Xia, C. Ming, Y. Han, L. Cao, J. Lu, P. Zhang, S. Zhang, H. Xu and Y.-Y. Sun, Semimetal or semiconductor: the nature of high intrinsic electrical conductivity in TiS<sub>2</sub>, *J. Phys. Chem. Lett.*, 2019, **10**, 6996–7001, DOI: 10.1021/acs.jpcclett.9b02710.
- 9 L. Zhang, D. Sun, J. Kang, H.-T. Wang, S.-H. Hsieh, W.-F. Pong, H. A. Bechtel, J. Feng, L.-W. Wang, E. J. Cairns and J. Guo, Tracking the chemical and structural evolution of the TiS<sub>2</sub> electrode in the lithium-ion cell using operando X-ray absorption spectroscopy, *Nano Lett.*, 2018, **18**, 4506–4515, DOI: 10.1021/acs.nanolett.8b01680.
- 10 B. Kartick, S. K. Srivastava and S. Mahanty, TiS<sub>2</sub>-MWCNT hybrid as high performance anode in lithium-ion battery, *J. Nanopart. Res.*, 2013, **15**, 1950, DOI: 10.1007/s11051-013-1950-5.
- 11 F. N. Sayed, M. B. Sreedhara, A. Soni, U. Bhat, R. Datta, A. J. Bhattacharyya and C. N. R. Rao, Li and Na-ion diffusion and intercalation characteristics in vertically aligned TiS<sub>2</sub> nanowall network grown using atomic layer deposition, *Mater. Res. Express*, 2019, **6**, 115549, DOI: 10.1088/2053-1591/ab3e19.
- 12 X. Zang, C. Shen, E. Kao, R. Warren, R. Zhang, K. S. Teh, J. Zhong, M. Wei, B. Li, Y. Chu, M. Sanghadasa, A. Schwartzberg and L. Lin, Titanium disulfide coated carbon nanotube hybrid electrodes enable high energy density symmetric pseudocapacitors, *Adv. Mater.*, 2018, **30**, 1704754, DOI: 10.1002/adma.201704754.
- 13 Z. Yang, S. Wang, K. Dong, Y. Dai and X. Lei, Electrochemical characterization of sulfur with low depth of charge/discharge in lithium sulfur batteries, *Electrochim. Acta*, 2016, **187**, 629–635, DOI: 10.1016/j.electacta.2015.11.116.
- 14 S. S. Zhang, A new finding on the role of LiNO<sub>3</sub> in lithium-sulfur battery, *J. Power Sources*, 2016, **322**, 99–105, DOI: 10.1016/j.jpowsour.2016.05.009.
- 15 H. Tan, S. Wang and X. Lei, New insights for the cyclic performance of Li/MnO<sub>2</sub> batteries using a simple electrochemical process, *J. Electrochem. Soc.*, 2015, **162**, A448–A452, DOI: 10.1149/2.0781503jes.
- 16 D. Y. Oh, Y. E. Choi, D. H. Kim, Y.-G. Lee, B. S. Kim, J. Park, H. Sohn and Y. S. Jung, All-solid-state lithium-ion batteries with TiS<sub>2</sub> nanosheets and sulphide solid electrolytes, *J. Mater. Chem. A*, 2016, **4**, 10329–10335, DOI: 10.1039/c6ta01628f.
- 17 J. Xu, J. Zhang, W. Zhang and C.-S. Lee, Interlayer nanoarchitectonics of two-dimensional transition-metal dichalcogenides nanosheets for energy storage and conversion applications, *Adv. Energy Mater.*, 2017, **7**, 1700571, DOI: 10.1002/aenm.201700571.
- 18 A. Van der Ven, J. Bhattacharya and A. A. Belak, Understanding Li diffusion in Li-intercalation compounds, *Acc. Chem. Res.*, 2013, **46**, 1216–1225, DOI: 10.1021/ar200329r.
- 19 S. N. Li, J. B. Liu and B. X. Liu, First principles study of nanostructured TiS<sub>2</sub> electrodes for Na and Mg ion storage, *J. Power Sources*, 2016, **320**, 322–331, DOI: 10.1016/j.jpowsour.2016.04.122.
- 20 W. Li, K. Wang, S. Cheng and K. Jiang, An ultrastable presodiated titanium disulfide anode for aqueous “rocking-chair” zinc ion battery, *Adv. Energy Mater.*, 2019, **9**, 1900993, DOI: 10.1002/aenm.201900993.
- 21 Z. Li, F. Du, X. Bie, D. Zhang, Y. Cai, X. Cui, C. Wang, G. Chen and Y. Wei, Electrochemical kinetics of the Li[Li<sub>0.23</sub>Co<sub>0.3</sub>Mn<sub>0.47</sub>]O<sub>2</sub> cathode material studied by GITT and EIS, *J. Phys. Chem. C*, 2010, **114**, 22751–22757, DOI: 10.1021/jp1088788.
- 22 T. P. Heins, N. Harms, L.-S. Schramm and U. Schröder, Development of a new electrochemical impedance spectroscopy approach for monitoring the solid electrolyte interphase formation, *Energy Technol.*, 2016, **4**, 1509–1513, DOI: 10.1002/ente.201600132.





- 23 Y. Teng, H. Zhao, Z. Zhang, Z. Li, Q. Xia, Y. Zhang, L. Zhao, X. Du, Z. Du, P. Lv and K. Świerczek, MoS<sub>2</sub> nanosheets vertically grown on graphene sheets for lithium-ion battery anodes, *ACS Nano*, 2016, **10**, 8526–8535, DOI: 10.1021/acsnano.6b03683.
- 24 J. Wu, Z. Lu, K. Li, J. Cui, S. Yao, M. I. Haq, B. Li, Q.-H. Yang, F. Kang, F. Ciucci and J.-K. Kim, Hierarchical MoS<sub>2</sub>/carbon microspheres as long-life and high-rate anodes for sodium-ion batteries, *J. Mater. Chem. A*, 2018, **6**, 5668–5677, DOI: 10.1039/c7ta11119c.
- 25 X. Xu, R. Zhao, B. Chen, L. Wu, C. Zou, W. Ai, H. Zhang, W. Huang and T. Yu, Progressively exposing active facets of 2D nanosheets toward enhanced pseudocapacitive response and high-rate sodium storage, *Adv. Mater.*, 2019, **31**, 1900526, DOI: 10.1002/adma.201900526.
- 26 X. Hu, J. Jia, G. Wang, J. Chen, H. Zhan and Z. Wen, Reliable and general route to inverse opal structured nanohybrids of carbon-confined transition metal sulfides quantum dots for high-performance sodium storage, *Adv. Energy Mater.*, 2018, **8**, 1801452, DOI: 10.1002/aenm.201801452.
- 27 J. Chen, Z.-L. Tao and S.-L. Li, Lithium intercalation in open-ended TiS<sub>2</sub> nanotubes, *Angew. Chem., Int. Ed.*, 2013, **42**, 2147–2151, DOI: 10.1002/anie.200250573.
- 28 X. Sun, P. Bonnick and L. F. Nazar, Layered TiS<sub>2</sub> positive electrode for Mg batteries, *ACS Energy Lett.*, 2016, **1**, 297–301, DOI: 10.1021/acsenergylett.6b00145.
- 29 Y. Liu, H. Wang, L. Cheng, N. Han, F. Zhao, P. Li, C. Jin and Y. Li, TiS<sub>2</sub> nanoplates: a high-rate and stable electrode material for sodium ion batteries, *Nano Energy*, 2016, **20**, 168–175, DOI: 10.1016/j.nanoen.2015.12.028.

